RESEARCH ARTICLE

Key Points:
- Foreshocks moved north with time, toward eventual mainshock location; seismicity rate did not accelerate leading up to mainshock
- Foreshocks ruptured adjacent areas along fault with little overlap; mainshock initiated where foreshocks locally increased stress
- Hector Mine foreshocks and mainshock were triggered by a cascade of stress transfer

Supporting Information:
- Supporting Information S1
- Data Set S1
- Data Set S2
- Data Set S3

Correspondence to:
C. E. Yoon,
claraeyoon@gmail.com

Foreshocks and Mainshock Nucleation of the 1999 M_w 7.1 Hector Mine, California, Earthquake

Clara E. Yoon[1] [iD], **Nana Yoshimitsu[1,2]** [iD], **William L. Ellsworth[1]** [iD], **and Gregory C. Beroza[1]** [iD]

[1]Department of Geophysics, Stanford University, Stanford, CA, USA, [2]Earthquake Research Institute, The University of Tokyo, Tokyo, Japan

Abstract Foreshocks provide valuable information on the nucleation process of an upcoming large earthquake. We applied high-resolution similar-waveform techniques for earthquake detection, location, and source parameter estimation to understand the space-time evolution of a foreshock sequence and its relationship to the mainshock hypocenter. The 1999 M_w 7.1 Hector Mine, California, earthquake was preceded by 50 foreshocks ($-0.4 \leq M \leq 3.7$) during the 20 hr before the mainshock. Foreshock activity did not accelerate leading up to the mainshock. Their locations moved north with time, rupturing adjacent areas along the fault plane with little overlap, but remained within a compact <2 km³ volume. The mainshock initiated at a location where previous foreshocks had locally increased the shear stress. These observations are consistent with a triggered cascade of stress transfer, where previous foreshocks load adjacent fault patches to rupture as additional foreshocks, and eventually the mainshock.

Plain Language Summary Foreshocks are smaller earthquakes that happen near, but before, a large earthquake. We can use foreshocks as a tool to help understand how large earthquakes begin. One model of earthquake initiation holds that small foreshocks directly trigger other small foreshocks by changing the stress on the fault and, eventually, a large earthquake occurs if the conditions are favorable. Since earthquakes of all sizes would start out the same way, it is impossible to predict ahead of time which earthquakes grow large. An alternative explanation holds that smaller foreshocks do not directly trigger the large earthquake but instead are a symptom of something else happening underground, such as slow fault movement that does not release ground-shaking waves. Several foreshocks occurred in the 20 hr before the 1999 magnitude 7.1 Hector Mine, California, earthquake. Analyzing records of the ground shaking from these foreshocks, we found that they are consistent with the former model, where each foreshock triggered the next one to happen like a line of falling dominoes. We discovered that the large earthquake started out the same way as the smaller foreshocks, so we could not tell ahead of time that it would eventually grow large.

1. Introduction

Foreshocks are smaller earthquakes that occur near the location of, but before, an eventual large earthquake, which is called the mainshock. About a quarter (Jones & Molnar, 1979; Reasenberg, 1999) to half (Abercrombie & Mori, 1996) of large earthquakes are observed to have foreshocks. When viewed in retrospect, foreshocks are the most obvious precursory signals to the mainshock, so it is important to understand them. Although foreshocks have been studied at the scale of laboratory stick slip experiments (McLaskey & Kilgore, 2013; McLaskey & Lockner, 2014; Ohnaka, 1993; Selvadurai & Glaser, 2017) as well as through direct seismological observations (Bouchon et al., 2011; Chen & Shearer, 2013; Dodge et al., 1995, 1996; Ellsworth & Bulut, 2018; Savage et al., 2017; Zanzerkia et al., 2003), there remains considerable debate on how large earthquakes nucleate and what foreshocks tell us about that process.

Earthquake nucleation is often explained in terms of two opposing end-member conceptual models: the cascade and the preslip models (Beroza & Ellsworth, 1996; Dodge et al., 1996; Ellsworth & Beroza, 1995; Fukao & Furumoto, 1985; Mignan, 2014). At one end, the cascade model says that foreshocks trigger other nearby foreshocks and eventually the mainshock, only through stress transfer, with earthquakes starting at local concentrations of increased stress. The cascade model holds that both small and large earthquakes initiate in the same way, without knowing ahead of time how large it will eventually get, which implies that earthquake prediction is effectively impossible (Beroza & Ellsworth, 1996; Ellsworth & Beroza, 1995).
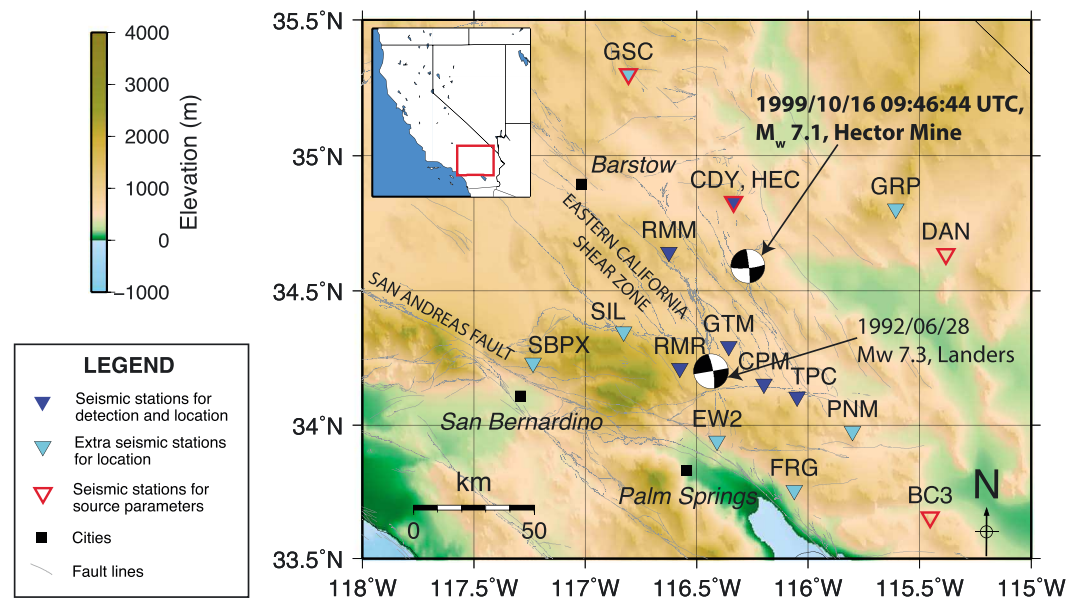
Figure 1. Map of southern California (red box, inset) with locations of the Hector Mine and Landers earthquakes shown by right-lateral focal mechanisms. Inverted triangles denote seismic stations used in foreshock detection (blue), location (blue and cyan), and source parameter calculation (red borders). We obtained Quaternary fault trace data from U.S. Geological Survey and California Geological Survey (2006) and topography data from Amante and Eakins (2009).

Observations of foreshocks before some large earthquakes have been interpreted to be consistent with the cascade model (e.g., Ellsworth & Bulut, 2018). The preslip model holds that the foreshocks are triggered by an underlying physical process, such as aseismic slip, that redistributes the stress along the fault. In this case, foreshocks are by-products of an underlying process, rather than directly responsible for triggering each other. The preslip model suggests that the area of the foreshocks may be related to the area of the underlying aseismic slip, so that the foreshocks contain predictive information about the size of the eventual mainshock (Dodge et al., 1996). There are other examples of large earthquakes where the foreshock activity is explained by the preslip model (Dodge et al., 1995, 1996). In addition, recent observations suggest that some large earthquakes preceded by foreshocks, especially in subduction zones, have been triggered by slow slip (Bouchon et al., 2013; Kato & Nakagawa, 2014; Kato et al., 2012; Radiguet et al., 2016; Ruiz et al., 2014).

The M_w 7.1 Hector Mine earthquake occurred on 16 October 1999 at 09:46:44 UTC (Figure 1), on a right-lateral strike-slip fault in the sparsely populated Mojave Desert in the Eastern California Shear Zone (ECSZ; Scientists of the U.S. Geological Survey et al., 2000). The ECSZ is a distributed region of north-northwest trending faults east of the San Andreas Fault, which accommodates about 25% of the relative plate motion between the Pacific and North American plates (Frankel et al., 2008). The recurrence interval between major earthquakes in the ECSZ can be thousands of years (Treiman et al., 2002). The Hector Mine earthquake was a complex rupture involving multiple faults; the central fault segment was well oriented for failure at N6° W, but the northernmost and southernmost faults were poorly oriented for failure at N35° W (Hauksson et al., 2002; Ji et al., 2002). The rupture initiated on a previously unknown north-trending structure and propagated bilaterally on a N6° W fault structure, later named the eastern branch of the Lavic Lake Fault (Hauksson et al., 2002; Ji et al., 2002). It then reached the surface, rupturing to the north along the western branch of the Lavic Lake Fault, as well as to the south along the Bullion Fault, in an arcuate pattern (Treiman et al., 2002).

Seven years before, the 28 June 1992 M_w 7.3 Landers earthquake ruptured a system of right-lateral strike-slip faults (Figure 1), located only 20–40 km from the eventual site of the Hector Mine earthquake (Hauksson et al., 1993, 2002; Ji et al., 2002). The Landers earthquake had a 28-event foreshock sequence in the 7 hr before the mainshock, which was inferred to result from an aseismic nucleation process (Dodge et al., 1995). Some studies suggested that the Landers earthquake triggered the Hector Mine earthquake, not by simple Coulomb stress transfer (Scientists of the U.S. Geological Survey et al., 2000) but possibly through viscoelastic flow in the ductile lower crust and upper mantle (Freed & Lin, 2001;

Zeng, 2001). Hauksson et al. (2002) and Chen and Shearer (2013) noted increased seismic activity near the eventual location of the Hector Mine earthquake immediately after the Landers earthquake.

The Hector Mine earthquake was preceded by 18 foreshocks with magnitudes $1.2 \leq M \leq 3.7$ (Data Set S1 in the supporting information) as detected by the Southern California Seismic Network (SCSN), during the 20 hr before the mainshock (Hauksson et al., 2002). Zanzerkia et al. (2003) manually inspected continuous seismic data to identify 42 foreshocks during these same 20 hr, precisely located them with the double-difference method (Waldhauser & Ellsworth, 2000), and found that the mainshock initiated on a different fault plane from the foreshocks; this study seeks to independently verify these results and to update them through more recent high-resolution methods developed to analyze seismicity. Chen and Shearer (2013) determined source parameters for the Hector Mine foreshocks and concluded that an aseismic transient triggered the Hector Mine earthquake, based on the similarity of the foreshock sequence to earthquake swarms in the area.

This study analyzes the relationship between the M_w 7.1 Hector Mine earthquake and its foreshock sequence, in order to understand the initiation process of the mainshock, and determine whether it is consistent with the cascade model or the preslip model of earthquake nucleation. We revisit this foreshock sequence with high-resolution seismological techniques, with a common theme of exploiting similar waveforms from pairs of nearby foreshocks. To improve the temporal resolution of the foreshocks, and determine if seismic activity increased leading up to the mainshock, we systematically detect foreshocks with similar waveforms using the Fingerprint and Similarity Thresholding (FAST) algorithm (Bergen et al., 2016; Rong et al., 2018; Yoon et al., 2015), inspired by recent data-mining techniques (Section 2). We then precisely locate the foreshocks and mainshock hypocenter with the double-difference algorithm (Waldhauser & Ellsworth, 2000), using differential travel times derived by cross-correlation between pairs of foreshock waveforms (Section 3). Afterward, we use the spectral ratio method (Huang et al., 2016; Imanishi & Ellsworth, 2006) to estimate reliable source parameters using pairs of similar foreshocks. Finally, assuming a circular fault rupture model, we examine the cumulative slip and stress change at the mainshock hypocenter from the eight largest foreshocks, to distinguish between competing models of earthquake nucleation (section 4).

2. Foreshock Detection

We first automatically detect as many of the smallest foreshocks as possible to improve the temporal resolution of the foreshock sequence. Continuous seismic data from the SCSN is available at the seven nearest stations (Figure 1, blue triangles) during the 20 hr immediately before the mainshock (Table S1), even though continuous data were not routinely collected and archived by the SCSN back in 1999. We complete a systematic, comprehensive search for foreshocks, using waveform similarity as a detection criterion, with the FAST earthquake detection method (Bergen & Beroza, 2018; Bergen et al., 2016; Rong et al., 2018; Yoon et al., 2015). This data set served as a test case for the newly developed FAST algorithm, which takes an unsupervised data-mining approach to identify earthquakes with similar waveforms in continuous data, without requiring prior knowledge of the desired signal. First, FAST independently runs on each component of continuous data at each station, with parameters in Table S2, to output a list containing pairs of times with similar earthquakes. We then combine the FAST outputs from each station through pair-wise pseudo-association (Bergen & Beroza, 2018), with parameters in Table S3, to detect earthquakes over the network of seven stations. Finally, we visually inspect waveforms of our detections to set empirical detection thresholds on the number of stations and the combined FAST similarity (Table S4). Through this procedure we detected a total of 50 foreshocks during the 20-hr time period, including all 18 foreshocks in the SCSN catalog (Data Set S1; Figure S1) and 32 uncataloged foreshocks (Data Sets S2 and S3; Figure S2), as well as three other earthquakes (Figure S3) and four false positive detections (Figure S4). The 50 foreshocks have similar waveforms at the nearest station HEC (Figure S5). In comparison, Zanzerkia et al. (2003) detected 42 foreshocks by visually inspecting the continuous data, which are all included in the 50 foreshocks detected by FAST. We computed magnitudes of the 32 uncataloged foreshocks, which range from −0.4 to 1.6, using the principal component relative-amplitude estimation method in Shelly et al. (2016), described in more detail in section S1. Figure 2a shows that the 32 smaller uncataloged foreshocks (blue) occur close in time to the 18 larger foreshocks in the catalog (red) and that the 5-hr quiet period between the two bursts of
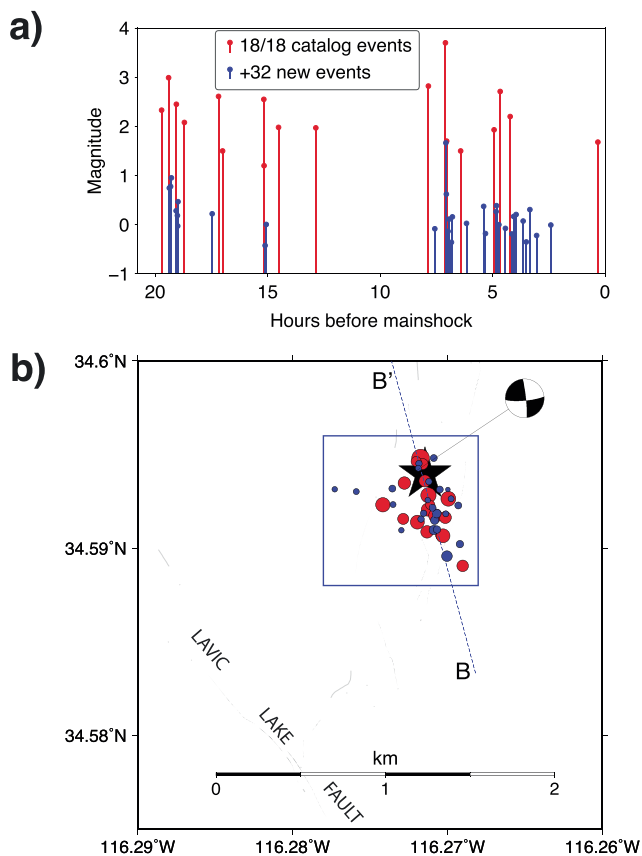
Figure 2. Overview of foreshock activity before Hector Mine earthquake: 18 catalog foreshocks from Southern California Seismic Network (red), 32 newly detected smaller foreshocks (blue), of which 24 are located. (a) Magnitude-time plot of foreshock activity. (b) Map view of foreshock sequence (circles sized by relative magnitude) and mainshock (hypocenter denoted by star) with focal mechanism (Hauksson et al., 2002), with Quaternary fault traces from U.S. Geological Survey and California Geological Survey (2006). The blue box indicates the region displayed in Figure 3a, and depth profiles B-B′ are shown in Figure 3b.

foreshock activity reported by Zanzerkia et al. (2003) remains intact. Foreshock activity did not accelerate immediately before the mainshock.

3. Foreshock Location

We relocate the 42 largest foreshocks and the mainshock using the double-difference location (hypoDD) algorithm (Waldhauser & Ellsworth, 2000) to increase the spatial resolution of the foreshock sequence and determine precisely the relative location between the foreshocks and mainshock hypocenter, since they have significant location and depth uncertainties in the existing catalogs (Figure S8). Section S2 includes full details of the location procedure (Deichmann & Garcia-Fernandez, 1992; Hauksson et al., 2012; Schaff et al., 2004; Trugman & Shearer, 2017). We use 14 stations to locate the foreshocks: the seven nearest stations already used for detection (Table S1; Figure 1, blue triangles) and seven additional stations located farther away (Table S5; Figure 1, cyan triangles). Inputs to hypoDD include P and S differential times computed between pairs of foreshocks on each station through a cross-correlation technique, as well as differential times between the P arrival at each foreshock and the initial amplitude rise (first 0.08 s after P arrival) of the mainshock, also obtained through cross-correlation. It is important to precisely locate the mainshock relative to the foreshocks, because a key question we want to answer is whether the mainshock initiated at a location of increased stress, or decreased stress, from the foreshock ruptures. If we cross-correlate an extended waveform around the P arrival for a large magnitude mainshock and a small magnitude foreshock, they would have low similarity and thus a low correlation coefficient, due to the presence of clipping in the mainshock waveform and differences in frequency content (Zanzerkia et al., 2003). However, if we limit the cross-correlation window to a short time (0.08 s) past the P arrival, the mainshock waveform would not be clipped, and we would match on the initial amplitude rise of both the mainshock and foreshock, which can be highly similar (Figure S7).

We run hypoDD with parameters from Table S6 and weights from Table S7, starting with the same initial location for all 42 foreshocks and the mainshock, with a 1-D layered velocity model from Kamer et al. (2017) (Table S8). We cannot constrain the absolute depth of these earthquakes because there are no nearby stations (Ji et al., 2002); the distance to the nearest station HEC is 26 km, which is at least several times their likely source depths. Therefore, we test five different trial depths, all plausible, for the starting location used in hypoDD: 3, 5, 8, 10, and 15 km (Figure S9), which are representative of the range of depths for these earthquakes reported in the literature (section S2). Location uncertainties are within the range of 10–120 m horizontally and 40–700 m vertically for most events. The location of the largest M 3.7 foreshock, which has P phases that are not as highly correlated with the other foreshocks, varies depending on the starting depth and has the largest uncertainty (up to ±1.2 km vertically). Although the relocated earthquake depths are dependent on the starting trial depth, we are primarily interested in observations of robust common features in the relative locations between the foreshocks and mainshock, which are insensitive to the assumed starting depth. In Figures 3 and 5, we report locations from the 8-km starting trial depth (Figure S9c).

The foreshocks and mainshock hypocenter are located on the eastern branch of the Lavic Lake Fault, which did not rupture to the surface (Figure 2b) (Hauksson et al., 2002; Ji et al., 2002; Treiman et al., 2002). Most foreshocks are located on a N10° W fault plane (Figures 2b and 3a), consistent with the orientation of one nodal plane of the mainshock focal mechanism (Hauksson et al., 2002), and the focal mechanisms for the largest foreshocks, which have considerable errors from 16° to 54° in fault plane orientation (Yang et al., 2012). The mainshock hypocenter is located on the same fault plane as the foreshocks (Figures 2b and 3a), which was also observed by Chen and Shearer (2013), but is inconsistent with Zanzerkia et al. (2003),
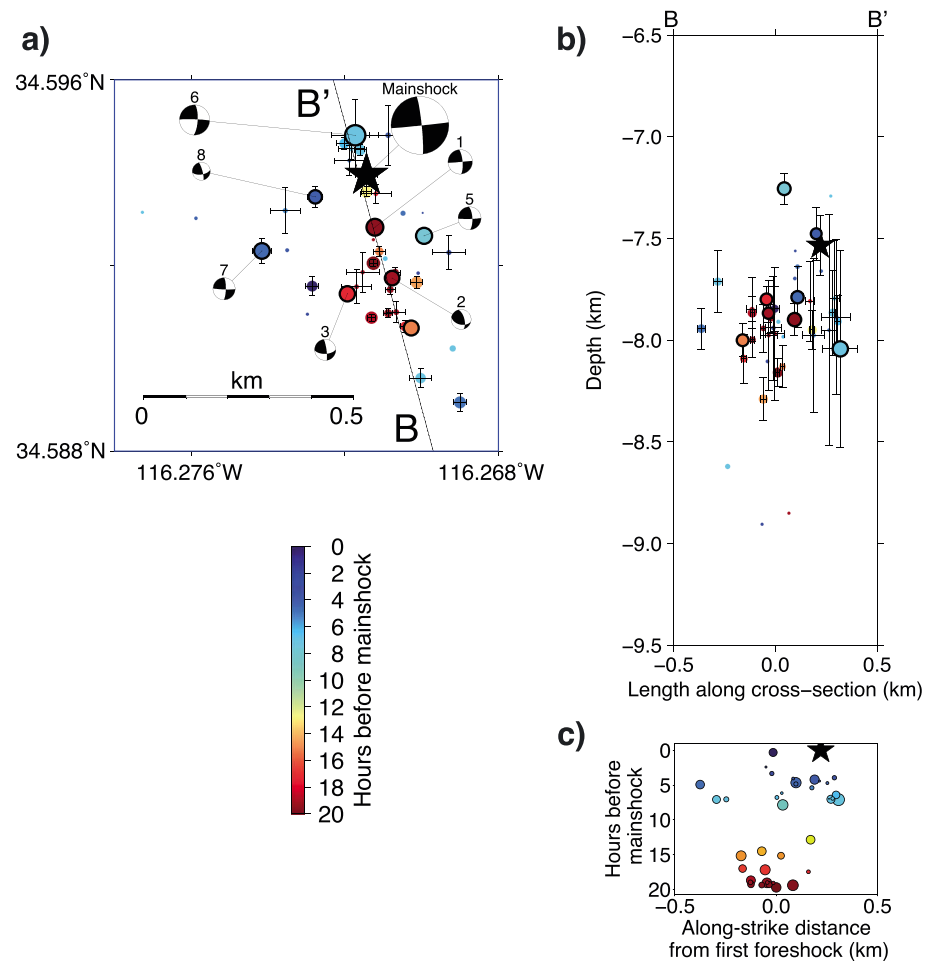
Figure 3. Space-time evolution of 42 located foreshocks (circles sized by relative magnitude, colored by time) of the Hector Mine earthquake (mainshock hypocenter denoted by star): (a) map view, (b) depth cross section along southeast-to-northwest profile B-B′ parallel to fault strike, and (c) along-strike time evolution of foreshocks leading up to mainshock. Locations were obtained with a trial starting depth of 8 km. Circles with thick edges in (a) and (b) indicate the eight largest foreshocks for which source parameters and rupture dimensions are calculated in Figure 5. In (a), the mainshock focal mechanism is from Hauksson et al. (2002), and the focal mechanisms for the eight largest foreshocks in Figure 5 (except for foreshock 4) are from Yang et al. (2012).

who found that the mainshock initiated about 0.5 km east of the fault plane containing the foreshocks. The foreshocks during 20–13 hr before the mainshock started tightly clustered together (red-orange circles, Figure 3). Starting 8 hr before the mainshock, the foreshocks migrated mostly to the north along the fault (Figure 3c; cyan-blue circles, Figure 3), although remaining in a compact <2-km³ volume. Some of the foreshocks in Figures 2b and 3a (foreshocks labeled as 3 and 7) are located along a conjugate fault plane striking ~60° northwest relative to the primary N10° W fault plane containing most of the foreshocks, although the existence of this conjugate fault plane is uncertain since it is not apparent in the foreshock locations from other trial starting depths such as 3, 5, and 15 km (Figure S9). The mainshock (black star, Figures 2b and 3) initiated near the north end of the foreshock zone, close to the later foreshocks.

4. Source Parameters and Slip Models of Largest Foreshocks

We extend our analysis beyond point source locations by estimating spectral source parameters for the eight largest foreshocks to model their rupture areas. From this we analyze how the slip and stress changes from each foreshock affect subsequent foreshocks and eventually the mainshock nucleation. Although the foreshock waveforms are similar, knowing their source dimensions allows us to distinguish between two possible scenarios: nonoverlapping ruptures of neighboring fault patches, which would support the cascade model; versus repeated rupture of the same fault patch, which would support the preslip model.
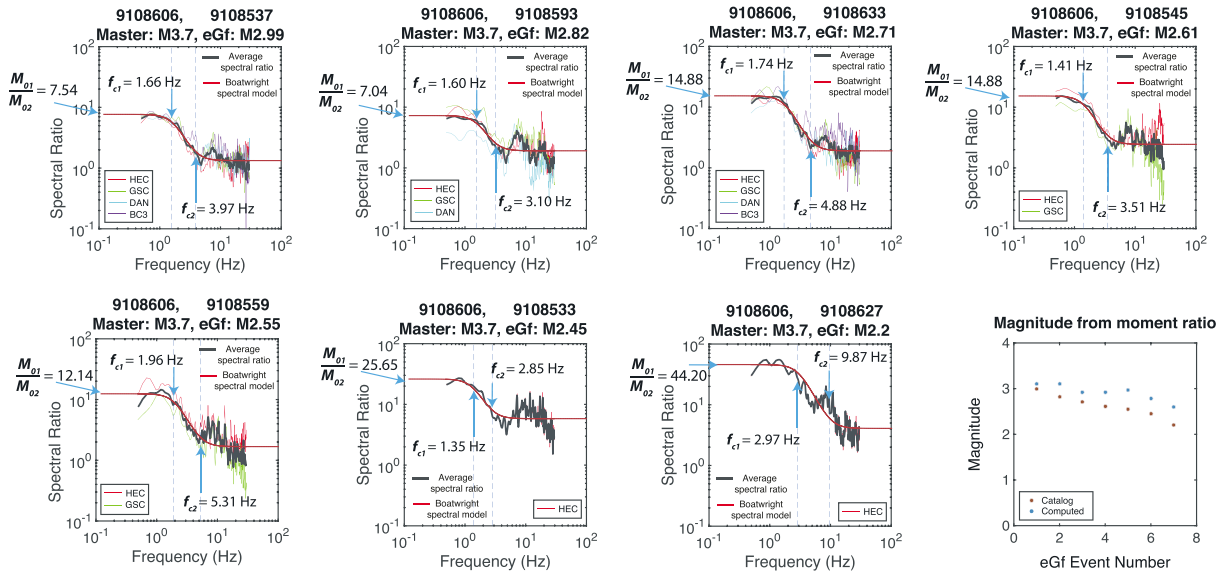
Figure 4. Source parameter estimation for eight largest foreshocks with an eGf approach, using the spectral ratio method (Imanishi & Ellsworth, 2006). Each plot has a spectral ratio estimate between the master event (always the M 3.7 largest foreshock with SCSN id 9108606) and a different eGf event (smaller foreshock with magnitude and SCSN id in title). Spectral ratio estimates at a given station that are above the signal-to-noise threshold (thin colored lines labeled by station) are used to calculate the average spectral ratio (thick gray line), which is fit to a Boatwright spectral model (equation 1, Boatwright (1980); thick red line) to estimate the master event corner frequency f_{c1}, eGf event corner frequency f_{c2}, and their ratio of seismic moments $M_r = M_{01}/M_{02}$. The lower right plot compares the M_w moment magnitudes calculated from the ratio of seismic moments (blue; Table 1, column 6) with the catalog magnitudes (red; Table 1, column 2) for all eGf events, assuming that $M_w = 3.7$ from the catalog for the master event. See section S3 for full details about the spectral ratio calculation and corner frequency estimation.

Ellsworth and Bulut (2018) performed a similar analysis of the four largest foreshocks preceding the 1999 M_w 7.1 Izmit, Turkey earthquake, which also had a right-lateral strike-slip mechanism, and determined that the foreshocks progressed unidirectionally as a series of linked ruptures to the mainshock. Their conclusion disagreed with Bouchon et al. (2011), who concluded that the waveform similarity of the Izmit foreshocks implied the existence of aseismic slip driving the mainshock.

We start by estimating the corner frequency f_c from the spectrum of the seismic source for each of the eight largest foreshocks ($2.2 \leq M \leq 3.7$), following the spectral ratio method (Huang et al., 2016; Imanishi & Ellsworth, 2006). This method is based on an empirical Green's function (eGf) approach, which uses two nearly colocated earthquakes with very similar waveforms, one larger (the master event) and one smaller (the eGf event), in order to cancel out path and site effects common to both earthquakes, leaving behind the source signature. At four SCSN broadband stations (Figure 1, red triangles; Table S9), we take a 10.24-s time window around the S arrival and compute the frequency spectrum for both earthquakes. We divide the spectrum of the master event by the spectrum of the eGf event to get the spectral ratio at each station, then compute the average spectral ratio over all stations (Figure 4, thick gray line). To estimate the corner frequencies f_{c1} and f_{c2} for the master and eGf events, respectively, and their seismic moment ratio $M_r = M_{01}/M_{02}$ (Figure 4), we fit the average spectral ratio to a Boatwright spectral model (Boatwright, 1980) with $\gamma = 2$:

$$\frac{u_1(f)}{u_2(f)} = \frac{M_{01}}{M_{02}} \left(\frac{1 + \left(\frac{f}{f_{c2}} \right)^{\gamma n}}{1 + \left(\frac{f}{f_{c1}} \right)^{\gamma n}} \right)^{\frac{1}{\gamma}}, \tag{1}$$

where f is frequency, $u_1(f)/u_2(f)$ is the average spectral ratio, $n = 2$ is the high-frequency falloff rate, and γ is a constant that controls the sharpness of the spectrum corner. Columns 3 and 4 in Table 1 contain f_c and $M_r = M_{01}/M_{02}$ estimates, respectively, for the eight largest foreshocks. Section S3 describes the spectral ratio calculation and corner frequency estimation in detail, while section S4 (Taylor, 1997) explains how we determined uncertainties for the f_c and M_r estimates and propagated these errors to the calculated source parameters in Table 1.

Table 1
Source Parameter Estimates for the Eight Largest Foreshocks (in Time Order)

SCSN event id	Magnitude SCSN catalog	Corner frequency f_c (Hz)	Moment ratio $M_r = M_{01}/M_{02}$	Seismic Moment M_0 (N m), from M_r	Magnitude from M_r	Source radius R (m)	Average slip D (cm)	Stress drop $\Delta\sigma$ (MPa)	Model assumption
9108537	2.99	3.97 ± 0.17	7.54 ± 0.53	(5.99 ± 0.42) ×10^{13}	3.12 ± 0.02	187 ± 15	1.81 ± 0.32	4.00 ± 1.03	$k = 0.21$ (Madariaga, 1976)
						330 ± 27	0.58 ± 0.10	0.73 ± 0.19	$k = 0.37$ (Brune, 1970)
						178	1.30	3	3 MPa stress drop
9108533	2.45	2.85 ± 0.12	25.65 ± 1.81	(1.76 ± 0.12) ×10^{13}	2.76 ± 0.02	261 ± 21	0.28 ± 0.05	0.43 ± 0.11	$k = 0.21$ (Madariaga, 1976)
						459 ± 38	0.09 ± 0.02	0.08 ± 0.02	$k = 0.37$ (Brune, 1970)
						96	0.70	3	3 MPa stress drop
9108545	2.61	3.51 ± 0.15	14.88 ± 1.12	(3.04 ± 0.23) ×10^{13}	2.92 ± 0.02	212 ± 17	0.72 ± 0.13	1.39 ± 0.36	$k = 0.21$ (Madariaga, 1976)
						373 ± 31	0.23 ± 0.04	0.26 ± 0.07	$k = 0.37$ (Brune, 1970)
						115	0.84	3	3 MPa stress drop
9108559	2.55	5.31 ± 0.22	12.14 ± 0.85	(3.72 ± 0.26) ×10^{13}	2.98 ± 0.02	140 ± 12	2.01 ± 0.36	5.92 ± 1.52	$k = 0.21$ (Madariaga, 1976)
						247 ± 20	0.65 ± 0.12	1.08 ± 0.28	$k = 0.37$ (Brune, 1970)
						107	0.78	3	3 MPa stress drop
9108593	2.82	3.10 ± 0.13	7.04 ± 0.50	(6.42 ± 0.45) ×10^{13}	3.14 ± 0.02	240 ± 20	1.18 ± 0.21	2.03 ± 0.52	$k = 0.21$ (Madariaga, 1976)
						423 ± 35	0.38 ± 0.07	0.37 ± 0.10	$k = 0.37$ (Brune, 1970)
						147	1.07	3	3 MPa stress drop
9108606	3.70	1.63 ± 0.07	1[a]	45.19 ×10^{13}[a]	3.70[a]	456 ± 38	2.30 ± 0.38	2.08 ± 0.52	$k = 0.21$ (Madariaga, 1976)
						804 ± 67	0.74 ± 0.12	0.38 ± 0.10	$k = 0.37$ (Brune, 1970)
						404	2.94	3	3 MPa stress drop
9108633	2.71	4.88 ± 0.21	14.88 ± 1.12	(3.04 ± 0.23) ×10^{13}	2.92 ± 0.02	152 ± 13	1.39 ± 0.25	3.77 ± 0.97	$k = 0.21$ (Madariaga, 1976)
						268 ± 22	0.45 ± 0.08	0.69 ± 0.18	$k = 0.37$ (Brune, 1970)
						129	0.94	3	3 MPa stress drop
9108627	2.20	9.87 ± 0.43	44.20 ± 3.11	(1.02 ± 0.07) ×10^{13}	2.60 ± 0.02	75 ± 6	1.91 ± 0.35	10.47 ± 2.72	$k = 0.21$ (Madariaga, 1976)
						133 ± 11	0.62 ± 0.11	1.91 ± 0.50	$k = 0.37$ (Brune, 1970)
						72	0.52	3	3 MPa stress drop

Note. Southern California Seismic Network (SCSN) event id (column 1) and magnitude (column 2) are from the SCSN catalog. Corner frequency f_c (column 3) and moment ratio M_r (column 4) are estimated from the spectral ratio method (Figure 4). For each foreshock, the source radius R (column 7), average slip D (column 8), and stress drop $\Delta\sigma$ (column 9) are calculated using three different model assumptions (column 10): (1) $k = 0.21$ (Madariaga (1976) rupture model), (2) $k = 0.37$ (Brune (1970) rupture model), (3) assume $\Delta\sigma = 3$ MPa stress drop. See section S4 for full details about the source parameter uncertainty estimates.
[a]For the largest foreshock, we used the catalog magnitude $M_w = 3.7$ to calculate its seismic moment M_{01} (column 5) using equation (S4). For the remaining seven foreshocks, we estimated the moment ratio M_r from the spectral ratios (Figure 4), then calculated the seismic moment $M_{02} = M_{01}/M_r$ (column 5).
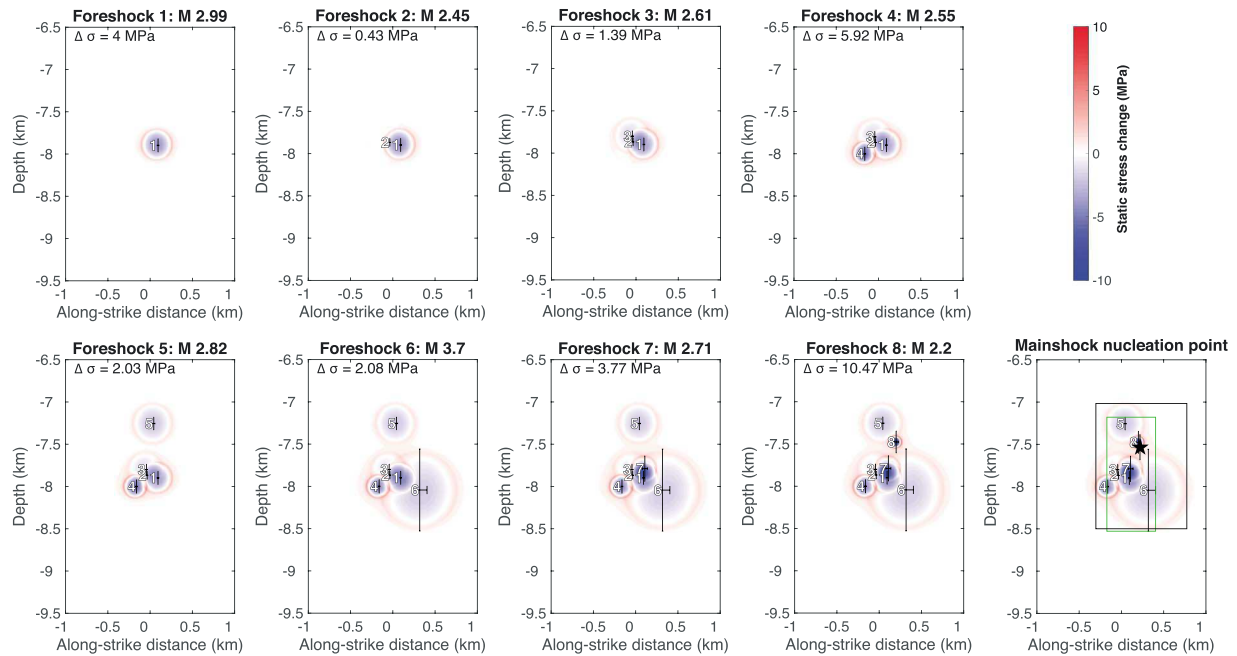
Figure 5. Cumulative static stress change (MPa) on fault plane from eight largest foreshocks in time order. Locations were obtained with a trial starting depth of 8 km (Figure 3). Source parameters (radius R, average slip D, constant stress drop $\Delta\sigma$ for the current foreshock in the upper left corner) for this figure were calculated using $k = 0.21$ (Madariaga, 1976), with parameters in Table 1. Models for slip (equation (5)) and the cumulative static stress change are from Andrews (1980). Foreshock locations (white numbers next to black error bars) and mainshock hypocenter (black star) are from Figure 3. In the last plot, the green rectangle is the smallest box containing all foreshock hypocenters including their uncertainties, while the black rectangle is the smallest box containing all foreshock rupture areas along the fault. It is possible that foreshocks 3 and 7 are located on a conjugate fault plane instead of the primary N10° W fault plane (Figure 3a), but this conjugate fault plane is not apparent in foreshock locations from other trial starting depths (Figure S9).

We assume a circular fault rupture model for the foreshocks, with radius R given by

$$R = \frac{kv_s}{f_c}, \tag{2}$$

where $v_s = (3.54 \pm 0.25)$ km/s for the S wave velocity at the 8-km foreshock depth (Table S8), f_c is the estimated corner frequency, and k is a constant that depends on the particular theoretical rupture model relating corner frequencies to the source dimension (Kaneko & Shearer, 2014). The uncertainty in v_s comes from the range of possible v_s values in the velocity model at the trial depths, from 3 km ($v_s = 3.29$ km/s) to 15 km ($v_s = 3.78$ km/s). We calculate the source radius for two end-member rupture models to represent a range of possible source dimensions. At one end, $k = 0.37$ for S waves in the Brune (1970) model, which is a kinematic model with instantaneous rupture within the circular crack. At the other extreme, $k = 0.21$ for S waves in the Madariaga (1976) model, which is a dynamic model with constant rupture velocity $0.9v_s$ propagating radially outward in the circular crack. This range of source dimensions includes intermediate values that may result from other rupture scenarios, such as Sato and Hirasawa (1973) ($k = 0.29$ for S waves) or Kaneko and Shearer (2014) ($k = 0.26$ for S waves). Column 7 in Table 1 has R values for the eight largest foreshocks.

The average slip D on the circular fault patch is

$$D = \frac{M_0}{\mu\pi R^2}, \tag{3}$$

where M_0 is the seismic moment, $\mu = 30$ GPa is the assumed shear modulus, and R is the source radius from equation (2). M_0 is computed directly from the catalog magnitude $M_w = 3.7$ for the largest foreshock, while M_0 is computed from the moment ratio $M_r = M_{01}/M_{02}$ estimates for the other seven foreshocks (section S3). Columns 5 and 8 in Table 1 contain M_0 and D values, respectively, for the eight largest foreshocks.

The static constant stress drop $\Delta\sigma$ within the circular fault patch (Eshelby, 1957) is

$$\Delta\sigma = \frac{7}{16}\frac{M_0}{R^3}. \tag{4}$$

For the eight largest foreshocks, the stress drops from the Brune (1970) model ($k = 0.37$) are relatively low, between 0.1 and 1.9 MPa, while the stress drops from the Madariaga (1976) model ($k = 0.21$) have more typical values ranging from 0.4 to 10.5 MPa (Table 1, column 9). These results are consistent with the low stress drops (median value 1.04 MPa) determined for these foreshocks by Chen and Shearer (2013), who used a different method to estimate corner frequencies.

We also calculate source dimensions using a third model, making the commonly used assumption of a $\Delta\sigma = 3$ MPa stress drop for each foreshock (e.g., Dodge et al., 1996). Setting M_w as the catalog magnitude (Table 1, column 2), we solve for the seismic moment M_0 using equation (S6), then use equation (2) to solve for the source radius R (Table 1, column 7), and subsequently compute the average slip D (Table 1, column 8). These R and D values, calculated assuming $\Delta\sigma = 3$ MPa, do not depend on the spectral ratio f_c and M_r estimates. Even if the f_c and M_r values estimated from the noisy spectral ratios in Figure 4 are inaccurate, the resulting R and D source parameters can be compared against those calculated with the $\Delta\sigma = 3$ MPa assumption.

For each foreshock, we model the slip within the circular fault rupture using this function from Andrews (1980):

$$d(r) = \begin{cases} D\left[1 - \left(\frac{r}{R}\right)^2\right]^{\frac{3}{2}} & r < R \\ 0 & r > R \end{cases}, \tag{5}$$

where r is the radius within the circular fault rupture, R is the source radius (equation (2)), and D is the average slip (equation (3)). The static shear stress change derived from this slip model does not have a non-physical singularity at the rupture edge (Andrews, 1980). With this model, each foreshock decreases the stress within the source radius, while the stress immediately outside the fault rupture increases locally but quickly decays with distance away from the rupture. This model, also used by Ellsworth and Bulut (2018) to study foreshocks of the Izmit earthquake, can help us examine how local stress changes from previous foreshocks influence later foreshocks and the mainshock.

We assume that the eight foreshocks with measured source dimensions and the mainshock hypocenter are located on the same fault plane, since our precise locations show that most foreshocks lie on a fault plane consistent with the mainshock focal mechanism (Figures 2b and 3a), and the largest foreshocks have similar focal mechanisms to each other and to the mainshock (Hauksson et al., 2002; Yang et al., 2012; Zanzerkia et al., 2003), with consistent first motions at the 14 stations used for location (Figure 1; Table S5). For each foreshock, we project its location onto the fault plane (Figure 3b), use equation (5) to model slip on a circular patch centered at this location, and calculate the resulting shear stress change (Andrews, 1980). We can do this because the double-difference location uncertainties (section 3) are comparable to, or smaller than, the source radius R estimates. It is possible that foreshocks 3 and 7 are located on a conjugate fault plane instead of the primary N10° W fault plane (Figure 3a), but this conjugate fault plane is not apparent in foreshock locations from other trial starting depths (Figure S9), so we consider the most general case that all eight largest foreshocks are on the N10° W fault plane.

Figure 5 shows the cumulative shear stress change along the fault from the eight largest foreshocks in time order, for a trial starting depth of 8 km (Figure 3), with source parameters calculated from the Madariaga (1976) model with $k = 0.21$ (Table 1). Most of the foreshocks rupture on a part of the fault adjacent to, but not overlapping with, ruptured areas from previous foreshocks, often initiating at a location where previous foreshocks have locally increased the stress (red), which is consistent with a cascade of stress transfer between neighboring foreshocks. Foreshocks 3 and 7 appear to be exceptions, rupturing almost the same fault patches as foreshocks 2 and 1 (blue), respectively, but if these events are located on the apparent conjugate fault plane striking ~60° northwest relative to the main N10° W fault plane (Figure 3a), there is very little overlap between rupture areas of previous foreshocks. Finally, the mainshock (black star, bottom right) nucleates just outside foreshock 8, at a local stress concentration around this compact, higher-stress-drop foreshock.

Figure S10 displays a more detailed uncertainty analysis of the cumulative shear stress changes from the eight largest foreshocks, and the eventual mainshock hypocenter, for different trial starting depths (each
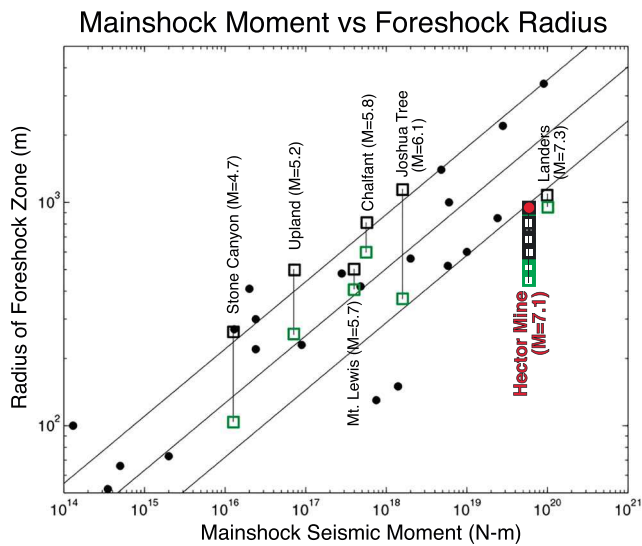
Figure 6. Observed scaling between foreshock area and mainshock size for six strike-slip earthquakes in California, modified from Dodge et al. (1996). This study adds a data point for the Hector Mine earthquake. Green squares indicate the area of the smallest rectangle containing all foreshock hypocenters including their uncertainties (green boxes for each trial starting depth for Hector Mine, Figure S10), while black squares show the area of the smallest rectangle containing all foreshock rupture areas along the fault (black boxes for each trial starting depth for Hector Mine, assuming the Madariaga, 1976, rupture model; Figure S10). The vertical axis plots the radius of the circle with the same area as these rectangles. The horizontal axis denotes the mainshock seismic moment, and thus magnitude. Black dots show estimates of source radius for other earthquakes from the Ellsworth and Beroza (1995) study of the seismic nucleation phase, and the red dot denotes the radius of the Hector Mine foreshocks as estimated by Chen and Shearer (2016). The diagonal straight lines are a least squares fit to the data and the 1σ boundaries from the fit by Dodge et al. (1996).

column: 3, 5, 8, 10, and 15 km) and source parameters calculated using different model assumptions (Table 1): two end-member rupture models from (a) the Madariaga (1976) model with $k = 0.21$ to (b) the Brune (1970) model with $k = 0.37$, as well as (c) the commonly assumed $\Delta\sigma = 3$ MPa stress drop. The location of foreshock 6, which is the largest foreshock (M 3.7) with a relatively low stress drop, varies depending on the trial starting depth. However, we make the following observations from the Madariaga (1976) model that are robust, regardless of the starting trial depth: Most of the foreshock rupture areas lie adjacent to each other with little overlap, and the mainshock hypocenter is located where previous foreshocks increased the shear stress. These observations are consistent with a cascade of stress transfer from foreshock to foreshock to mainshock. In contrast, with the Brune (1970) model, the slip is spread out over a larger area, so the peak cumulative slip and stress drops are lower, there is some degree of overlap between foreshock rupture areas, and the mainshock sometimes (though not always) nucleates in an area where previous foreshocks have reduced the stress. However, we prefer the Madariaga (1976) model for our interpretations, because it is a more realistic dynamic model with a finite rupture propagation velocity, than the Brune (1970) model, which assumes instantaneous rupture propagation. The foreshock rupture areas determined from the $\Delta\sigma = 3$ MPa stress drop assumption, which are completely independent of the spectral ratio estimates in Figure 4, closely resemble the rupture areas from our preferred Madariaga (1976) model with comparable stress change levels; our observation of adjacent rupture areas with little overlap, with the mainshock nucleating at a location of increased shear stress, remains valid.

5. Discussion

The M_w 7.1 Hector Mine mainshock nucleated at a location along the fault that had been loaded by a sequence of several foreshocks in the previous 20 hr; the simplest explanation, and our preferred interpretation, for this earthquake sequence is that they triggered each other through a cascade of stress transfer. This observation holds regardless of the starting trial depth, so the interpretation is robust despite the uncertainty in absolute depth. It is not necessary to invoke aseismic slip nor high fluid pressure to explain the foreshocks and mainshock nucleation process for the Hector Mine earthquake. However, given existing observations of these earthquakes, we cannot rule out these external physical driving mechanisms either. No independent geodetic observations of aseismic slip before the Hector Mine earthquake have been measured, but it is possible that aseismic slip below the geodetic detection threshold of M_w 4.5 may have been present (Mellors et al., 2002; Roeloffs, 2006). In contrast to our interpretation, Chen and Shearer (2013) inferred that the Hector Mine foreshocks and mainshock were triggered by an underlying aseismic transient, since these earthquakes had similar characteristics to other swarms in the ECSZ thought to be triggered by fluid flow: systematic spatiotemporal migration of the foreshocks with diffusion-like speed, and low stress drops. Based on a statistical analysis of earthquake catalogs, Chen and Shearer (2016) argued that foreshocks of $M \geq 5$ earthquakes in California (including the Hector Mine earthquake) are independent of mainshock nucleation processes, whether cascading or aseismic, and that it is difficult to distinguish foreshocks from random clusters of small earthquakes that do not culminate in a large mainshock. Regardless of the physical triggering mechanism for the Hector Mine earthquake and its foreshocks, the question of how and why the rupture sometimes gets large, and sometimes does not, remains.

Dodge et al. (1996) observed a scaling relationship between the radius of the area covered by the foreshocks and the seismic moment of the eventual mainshock for six strike-slip earthquakes in California (Figure 6), which is consistent with the preslip model, where foreshocks are by-products of aseismic slip in the

earthquake nucleation process. Chen and Shearer (2016) revisited this scaling relationship by analyzing 14 mainshocks in California with swarm-like foreshock sequences, including the Hector Mine earthquake. Although their estimate of the Hector Mine foreshock radius (Figure 6, red dot) agreed with this scaling relationship, they ultimately concluded, based on the rest of their foreshock-mainshock data, that the foreshock area has no correlation with the eventual mainshock magnitude and furthermore that foreshocks are independent of the mainshock nucleation process. We find that the radius for the Hector Mine foreshocks, calculated from the models in Figure S10a for the full range of starting trial depths, is inconsistent with the Dodge et al. (1996) scaling relationship (Figure 6); the foreshock area is much smaller than expected for an eventual M_w 7.1 mainshock, lying outside the 1σ boundaries of the least squares fit that defines the scaling relationship. This observation provides additional evidence to support the "cascade model" for foreshocks and mainshock nucleation for Hector Mine.

This study is limited by the lack of near seismic stations needed to resolve key details about the foreshock rupture areas and their relationship to the mainshock (Figure 1). Without nearby stations (the nearest station HEC is 26 km away), we have uncertain depth estimates for the foreshocks and mainshock hypocenter. Without additional constraints, we estimate source dimensions for the foreshocks using circular fault patches (Figure 5), with a limited number of broadband stations that are not adversely affected by clipping or excessive noise (Figure 4). If we had a denser seismic network with more stations located near the foreshocks, we could get more detailed fault structure information (Ruhl et al., 2016; Savage et al., 2017) and more precise source parameter estimates from a circular fault model (Ruhl et al., 2017). If we had finite slip distributions of the Hector Mine foreshocks, they might resolve the heterogeneous stress distribution on the fault with greater detail, which could constrain our interpretation. For example, two different studies of the M 4.3 foreshock to the 1992 M_w 6.1 Joshua Tree, California, earthquake reached opposite conclusions; Dodge et al. (1996) used circular fault models and a range of plausible fault dimensions to conclude that the Joshua Tree mainshock ruptured the same part of the fault as its foreshock, while Mori (1996) calculated a finite slip model for the foreshock and concluded that the Joshua Tree mainshock rupture was adjacent to, but did not overlap, the foreshock rupture zone. When in the future a foreshock sequence to a large earthquake is captured by a dense "large-N" seismic network with hundreds of stations (Li et al., 2018), there will be potential for imaging small foreshocks down to magnitude 2 or below with finite fault models, which would advance our understanding of the relationship between foreshocks and mainshock nucleation. Independent near-field geodetic observations of aseismic slip and measurements of fluid pressure would also be necessary to determine to what extent these potential triggering mechanisms are involved.

Due to observational limitations, our study assumed that the foreshocks occurred on either a single vertical fault plane, or on two conjugate vertical fault planes, but we cannot rule out the possibility that they happened on different subparallel fault structures in a distributed damage zone (Savage et al., 2017). Fault zone complexity and heterogeneity have been associated with foreshocks (Dodge et al., 1996). Cheng and Wong (2016) found that foreshocks to large strike-slip earthquakes are more likely if an extensional bridge zone heterogeneity exists between two subparallel fault structures, which is true for the complex Hector Mine earthquake rupture (Hauksson et al., 2002; Ji et al., 2002; Treiman et al., 2002). Chen and Shearer (2016) found that foreshocks in California are more likely to occur at extensional stepovers, high heat flow regions, and complex fault zones.

6. Conclusions

This study exploits waveform similarity among earthquakes to detect, precisely locate, and reliably estimate source parameters for foreshocks of the 1999 M_w 7.1 Hector Mine earthquake. We found that 50 foreshocks occurred in the 20 hr before the mainshock, including 32 small uncataloged foreshocks with magnitudes −0.4 to 1.6 (Figure 2a), without any acceleration of foreshock activity leading up to the mainshock. The 42 largest foreshocks, located on a N10° W fault plane consistent with the mainshock focal mechanism (Figures 2b and 3a), moved north with time but remained within a compact <2-km³ volume (Figure 3). The mainshock initiated at the north end of the foreshock zone, along the same fault plane as the foreshocks (Figures 2b and 3), contrary to Zanzerkia et al. (2003) who located the mainshock hypocenter on a different fault from the foreshocks. Finite source modeling of the cumulative slip and stress changes from the eight largest foreshocks ($2.2 \leq M \leq 3.7$), assuming a circular rupture model, revealed that their rupture areas adjoined each other but did not overlap much. The mainshock initiated at a location where the stress had increased locally, having been loaded by previous foreshock ruptures. These observations can be explained

by a simple cascade model of earthquake nucleation, where the foreshocks trigger neighboring foreshocks by transferring stress to adjacent fault patches and eventually trigger the mainshock that grows large. Our interpretation does not require the existence of an underlying physical process, such as aseismic slip or fluid flow, to influence the Hector Mine foreshocks and mainshock; observational evidence of these processes is lacking (although they cannot be ruled out), and the foreshock area is smaller than expected for a M_w 7.1 earthquake triggered by aseismic slip (Figure 6). Future progress in understanding foreshock sequences and large earthquake nucleation requires improved observations, including denser nearby seismic networks to enable detailed finite source imaging of foreshock sequences.

References

Abercrombie, R. E., & Mori, J. (1996). Occurrence patterns of foreshocks to large earthquakes in the western United States. *Nature*, *381*, 303–307. https://doi.org/10.1038/381303a0

Amante, C., & Eakins, B. W. (2009). ETOPO1 1 Arc-Minute Global Relief Model: Procedures, data sources and analysis (NOAA Technical Memorandum NESDIS NGDC-24). Maryland, United States: National Geophysical Data Center, NOAA. https://doi.org/10.7289/V5C8276M, (accessed 2018-03-07).

Andrews, D. J. (1980). A stochastic fault model 1. Static case. *Journal of Geophysical Research*, *85*(B7), 3867–3877. https://doi.org/10.1029/JB085iB07p03867

Bergen, K. J., & Beroza, G. C. (2018). Detecting earthquakes over a seismic network using single-station similarity measures. *Geophysical Journal International*, *213*(3), 1984–1998. https://doi.org/10.1093/gji/ggy100

Bergen, K. J., & Beroza, G. C. (2018). Earthquake fingerprints: Extracting waveform features for similarity-based earthquake detection. *Pure and Applied Geophysics*, 1–23. https://doi.org/10.1007/s00024-018-1995-6

Bergen, K., Yoon, C., & Beroza, G. C. (2016). Scalable similarity search in seismology: A new approach to large-scale earthquake detection. *Proceedings of the 9th International Conference on Similarity Search and Applications*, 301–308. https://doi.org/10.1007/978-3-319-46759-7_23

Beroza, G. C., & Ellsworth, W. L. (1996). Properties of the seismic nucleation phase. *Tectonophysics*, *261*, 209–227. https://doi.org/10.1016/0040-1951(96)00067-4

Beyreuther, M., Barsch, R., Kischer, L., Megies, T., Behr, Y., & Wassermann, J. (2010). ObsPy: A Python toolbox for seismology. *Seismological Research Letters*, *81*(3), 530–533. https://doi.org/10.1785/gssrl.81.3.530

Boatwright, J. (1980). A spectral theory for circular seismic sources: Simple estimates of source dimension, dynamic stress drop, and radiated seismic energy. *Bulletin of the Seismological Society of America*, *70*, 1–28.

Bouchon, M., Durand, V., Marsan, D., Karabulut, H., & Schmittbuhl, J. (2013). The long precursory phase of most large interplate earthquakes. *Nature Geoscience*, *6*, 299–302. https://doi.org/10.1038/ngeo1770

Bouchon, M., Karabulut, H., Aktar, M., Ozalaybey, S., Schmittbuhl, J., & Bouin, M. P. (2011). Extended nucleation of the 1999 M_w 7.6 Izmit Earthquake. *Science*, *331*, 877–880. https://doi.org/10.1126/science.1197341

Brune, J. (1970). Tectonic stress and the spectra of seismic shear waves from earthquakes. *Journal of Geophysical Research*, *75*, 4997–5009. https://doi.org/10.1029/JB075i026p04997

Chen, X., & Shearer, P. M. (2013). California foreshock sequences suggest aseismic triggering process. *Geophysical Research Letters*, *40*, 1–6. https://doi.org/10.1002/grl.50444

Chen, X., & Shearer, P. M. (2016). Analysis of foreshock sequences in California and implications for earthquake Triggering. *Pure and Applied Geophysics*, *173*, 133–152. https://doi.org/10.1007/s00024-015-1103-0

Cheng, Y., & Wong, L. N. Y. (2016). Occurrence of foreshocks in large earthquakes with strike-slip rupturing. *Bulletin of the Seismological Society of America*, *106*(1), 213–224. https://doi.org/10.1785/0120140338

Deichmann, N., & Garcia-Fernandez, M. (1992). Rupture geometry from high-precision relative hypocentre locations of microearthquake clusters. *Geophysical Journal International*, *110*, 501–517.

Dodge, D. A., Beroza, G. C., & Ellsworth, W. L. (1995). Foreshock sequence of the 1992 Landers, California, earthquake and its implications for earthquake nucleation. *Journal of Geophysical Research*, *100*(B7), 9865–9880. https://doi.org/10.1029/95JB00871

Dodge, D. A., Beroza, G. C., & Ellsworth, W. L. (1996). Detailed observations of California foreshock sequences: Implications for the earthquake initiation process. *Journal of Geophysical Research*, *101*(B10), 22,371–22,392. https://doi.org/10.1029/96JB02269

Ellsworth, W. L., & Beroza, G. C. (1995). Seismic evidence for an earthquake nucleation phase. *Science*, *268*, 851–855. https://doi.org/10.1126/science.268.5212.851

Ellsworth, W. L., & Bulut, F. (2018). Nucleation of the 1999 Izmit earthquake by a triggered cascade of foreshocks. *Nature Geoscience*, *11*, 531–535. https://doi.org/10.1038/s41561-018-0145-1

Eshelby, J. D. (1957). The determination of the elastic field of an ellipsoidal inclusion, and related problems. *Proceedings of the Royal Society of London A*, *241*(1226), 376–396. https://doi.org/10.1098/rspa.1957.0133

Frankel, K. L., Glazner, A. F., Kirby, E., Monastero, F. C., Strane, M. D., Oskin, M. E., et al. (2008). Active tectonics of the eastern California shear zone. In E. M. Duebendorfer & E. I. Smith (Eds.), *Field Guide to Plutons, Volcanoes, Faults, Reefs, Dinosaurs, and Possible Glacia- tion in Selected Areas of Arizona, California, and Nevada* (Vol. 11, pp. 43–81). Boulder, CO: Geological Society of America Field Guide. https://doi.org/10.1130/2008.fld011(03)

Freed, A. M., & Lin, J. (2001). Delayed triggering of the 1999 Hector Mine earthquake by viscoelastic stress transfer. *Nature*, *411*, 180–183. https://doi.org/10.1038/35075548

Fukao, Y., & Furumoto, M. (1985). Hierarchy in earthquake size distribution. *Physics of the Earth and Planetary Interiors*, *37*, 149–168. https://doi.org/10.1016/0031-9201(85)90048-2

Hauksson, E., Jones, L. M., & Hutton, K. (2002). The 1999 M_w 7.1 Hector Mine, California, earthquake sequence: Complex conjugate strike-slip faulting. *Bulletin of the Seismological Society of America*, *92*(4), 1154–1170. https://doi.org/10.1785/0120000920

Hauksson, E., Jones, L. M., Hutton, K., & Eberhart-Phillips, D. (1993). The 1992 Landers earthquake sequence: Seismological observations. *Journal of Geophysical Research*, *98*(B11), 19,835–19,858. https://doi.org/10.1029/93JB02384

Hauksson, E., Yang, W., & Shearer, P. M. (2012). Waveform relocated earthquake catalog for Southern California (1981 to June 2011). *Bulletin of the Seismological Society of America*, *102*(5), 2239–2244. https://doi.org/10.1785/0120120010

Helffrich, G., Wookey, J., & Bastow, I. (2013). *The seismic analysis code: A primer and user's guide* (1st ed.). United Kingdom: Cambridge University Press.

Huang, Y., Beroza, G. C., & Ellsworth, W. L. (2016). Stress drop estimates of potentially induced earthquakes in the Guy-Greenbrier sequence. *Journal of Geophysical Research: Solid Earth*, *121*, 6597–6607. https://doi.org/10.1002/2016JB013067

Imanishi, K., & Ellsworth, W. L. (2006). Source scaling relationships of microearthquakes at Parkfield, CA, Determined Using the SAFOD Pilot Hole Seismic Array. In R. E. Abercrombie, A. McGarr, H. Kanamori, & G. Di Toro (Eds.), *Earthquakes: Radiated energy and the physics of earthquake faulting, Geophysical Monograph Series* (Vol. 170, pp. 81–90). Washington, DC: American Geophysical Union. https://doi.org/10.1029/170GM10

Ji, C., Wald, D. J., & Helmberger, D. V. (2002). Source description of the 1999 Hector Mine, California, earthquake, part II: Complexity of slip history. *Bulletin of the Seismological Society of America*, *92*(4), 1208–1226. https://doi.org/10.1785/0120000917

Jones, L. M., & Molnar, P. (1979). Some characteristics of foreshocks and their possible relationship to earthquake prediction and premonitory slip on faults. *Journal of Geophysical Research*, *84*(B7), 3596–3608. https://doi.org/10.1029/JB084iB07p03596

Kamer, Y., Kissling, E., Ouillon, G., & Sornette, D. (2017). KaKiOS-16: A probabilistic, nonlinear, absolute location catalog of the 1981–2011 Southern California seismicity. *Bulletin of the Seismological Society of America*, *107*(5), 1994–2007. https://doi.org/10.1785/0120160146

Kaneko, Y., & Shearer, P. M. (2014). Seismic source spectra and estimated stress drop derived from cohesive-zone models of circular subshear rupture. *Geophysical Journal International*, *197*, 1002–1015. https://doi.org/10.1093/gji/ggu030

Kato, A., & Nakagawa, S. (2014). Multiple slow-slip events during a foreshock sequence of the 2014 Iquique, Chile M_w 8.1 earthquake. *Geophysical Research Letters*, *41*, 5420–5427. https://doi.org/10.1002/2014GL061138

Kato, A., Obara, K., Igarashi, T., Tsuruoka, H., Nakagawa, S., & Hirata, N. (2012). Propagation of slow slip leading up to the 2011 M_w 9.0 Tohoku-Oki earthquake. *Science*, *355*, 705–708. https://doi.org/10.1126/science.1215141

Li, Z., Peng, Z., Hollis, D., Zhu, L., & McClellan, J. (2018). High-resolution seismic event detection using local similarity for Large-N arrays. *Nature Scientific Reports*, *8*, 1646. https://doi.org/10.1038/s41598-018-19728-w

Madariaga, R. (1976). Dynamics of an expanding circular fault. *Bulletin of the Seismological Society of America*, *66*, 639–666.

McLaskey, G. C., & Kilgore, B. D. (2013). Foreshocks during the nucleation of stick-slip instability. *Journal of Geophysical Research: Solid Earth*, *118*, 2982–2997. https://doi.org/10.1002/jgrb.50232

McLaskey, G. C., & Lockner, D. A. (2014). Preslip and cascade processes initiating laboratory stick slip. *Journal of Geophysical Research: Solid Earth*, *119*, 6323–6336. https://doi.org/10.1002/2014JB011220

Mellors, R. J., Sichoix, L., & Sandwell, D. T. (2002). Lack of precursory slip to the 1999 Hector Mine, California, earthquake as constrained by InSAR. *Bulletin of the Seismological Society of America*, *92*(4), 1443–1449.

Mignan, A. (2014). The debate on the prognostic value of earthquake foreshocks: A meta-analysis. *Nature Scientific Reports*, *4*, 4099. https://doi.org/10.1038/srep04099

Mori, J. (1996). Rupture directivity and slip distribution of the M 4.3 foreshock to the 1992 Joshua Tree earthquake, Southern California. *Bulletin of the Seismological Society of America*, *86*(3), 805–810.

Ohnaka, M. (1993). Critical size of the nucleation zone of earthquake rupture inferred from immediate foreshock activity. *Journal of Physics of the Earth*, *41*, 45–56. https://doi.org/10.4294/jpe1952.41.45

Radiguet, M., Perfettini, H., Cotte, N., Gualandi, A., Valette, B., Kostoglodov, V., et al. (2016). Triggering of the 2014 M_w 7.3 Papanoa earthquake by a slow slip event in Guerrero, Mexico. *Nature Geoscience*, *9*, 829–834. https://doi.org/10.1038/ngeo2817

Reasenberg, P. A. (1999). Foreshock occurrence before large earthquakes. *Journal of Geophysical Research*, *104*(B3), 4755–4768. https://doi.org/10.1029/1998JB900089

Roeloffs, E. A. (2006). Evidence for aseismic deformation rate changes prior to earthquakes. *Annual Review of Earth and Planetary Sciences*, *34*, 591–627. https://doi.org/10.1146/annurev.earth.34.031405.124947

Rong, K., Yoon, C. E., Bergen, K. J., Elezabi, H., Bailis, P., Levis, P., & Beroza, G. C. (2018). Locality-sensitive hashing for earthquake detection: A case study scaling data-driven science [Innovative Systems and Applications]. *PVLDB*, *11*, 5. arXiv:1803.09835, https://doi.org/10.14778/3236187.3236214

Ruhl, C. J., Abercrombie, R. E., & Smith, K. D. (2017). Spatiotemporal variation of stress drop during the 2008 Mogul, Nevada, earthquake swarm. *Journal of Geophysical Research: Solid Earth*, *122*, 8163–8180. https://doi.org/10.1002/2017JB014601

Ruhl, C. J., Abercrombie, R. E., Smith, K. D., & Zaliapin, I. (2016). Complex spatiotemporal evolution of the 2008 M_w 4.9 Mogul earthquake swarm (Reno, Nevada): Interplay of fluid and faulting. *Journal of Geophysical Research: Solid Earth*, *121*, 8196–8216. https://doi.org/10.1002/2016JB013399

Ruiz, S., Metois, M., Fuenzalida, A., Ruiz, J., Leyton, F., Grandin, R., et al. (2014). Intense foreshocks and a slow slip event preceded the 2014 Iquique M_w 8.1 earthquake. *Science*, *345*, 1165–1169. https://doi.org/10.1126/science.1256074

Sato, T., & Hirasawa, T. (1973). Body wave spectra from propagating shear cracks. *Journal of Physics of the Earth*, *21*, 415–431. https://doi.org/10.4294/jpe1952.21.415

Savage, H. M., Keranen, K. M., Schaff, D. P., & Dieck, C. (2017). Possible precursory signals in damage zone foreshocks. *Geophysical Research Letters*, *44*, 5411–5417. https://doi.org/10.1002/2017GL073226

Schaff, D. P., Bokelmann, G. H. R., Ellsworth, W. L., Zanzerkia, E., Waldhauser, F., & Beroza, G. C. (2004). Optimizing correlation techniques for improved earthquake location. *Bulletin of the Seismological Society of America*, *94*(2), 705–721.

Scientists of the U.S. Geological Survey, Southern California Earthquake Center, & California Division of Mines and Geology (2000). Preliminary report on the 10/16/1999 *M* 7.1 Hector Mine, California earthquake. *Seismological Research Letters*, *71*(1), 11–23. https://doi.org/10.1785/gssrl.71.1.11

Selvadurai, P. A., & Glaser, S. D. (2017). Asperity generation and its relationship to seismicity on a planar fault: A laboratory simulation. *Geophysical Journal International*, *208*, 1009–1025. https://doi.org/10.1093/gji/ggw439

Shelly, D. R., Ellsworth, W. L., & Hill, D. P. (2016). Fluid-faulting evolution in high definition: Connecting fault structure and frequency-magnitude variations during the 2014 Long Valley Caldera, California, earthquake swarm. *Journal of Geophysical Research: Solid Earth*, *121*, 1776–1795. https://doi.org/10.1002/2015JB012719

Southern California Earthquake Center (2013). Caltech. Dataset. https://doi.org/10.7909/C3WD3xH1, http://scedc.caltech.edu/about/citation.html

Taylor, J. R. (1997). *An introduction to error analysis: The study of uncertainties in physical measurements* (2nd ed.). Mill Valley, CA: University Science Books.

Treiman, J. A., Kendrick, K. J., Bryant, W. A., Rockwell, T. K., & McGill, S. F. (2002). Primary surface rupture associated with the M_w 7.1 16 October 1999 Hector Mine earthquake, San Bernardino County, California. *Bulletin of the Seismological Society of America*, *92*(4), 1171–1191. https://doi.org/10.1785/0120000923

Trugman, D. T., & Shearer, P. M. (2017). GrowClust: A hierarchical clustering algorithm for relative earthquake relocation, with application to the Spanish Springs and Sheldon, Nevada, Earthquake Sequences. *Seismological Research Letters*, *88*(2A), 379–391. https://doi.org/10.1785/0220160188

U.S. Geological Survey, & California Geological Survey (2006). Quaternary fault and fold database for the United States, accessed. Retrieved from https://earthquake.usgs.gov/hazards/qfaults/, (accessed Mar 7, 2018).

Waldhauser, F., & Ellsworth, W. L. (2000). A double-difference earthquake location algorithm: Method and application to the Northern Hayward Fault, California. *Bulletin of the Seismological Society of America*, *90*(6), 1353–1368.

Wessel, P., Smith, W. H. F., Scharroo, R., Luis, J. F., & Wobbe, F. (2013). Generic mapping tools: Improved version released. *Eos, Transactions American Geophysical Union*, *94*, 409–410. https://doi.org/10.1002/2013EO450001

Yang, W., Hauksson, E., & Shearer, P. M. (2012). Computing a large refined catalog of focal mechanisms for Southern California (1981-2010): Temporal stability of the style of faulting. *Bulletin of the Seismological Society of America*, *102*(3), 1179–1194. https://doi.org/10.1785/0120110311

Yoon, C. E., O'Reilly, O., Bergen, K. J., & Beroza, G. C. (2015). Earthquake detection through computationally efficient similarity search. *Science Advances*, *E1501057*, 1. https://doi.org/10.1126/sciadv.1501057

Zanzerkia, E. E., Beroza, G. C., & Vidale, J. E. (2003). Waveform analysis of the 1999 Hector Mine foreshock sequence. *Geophysical Research Letters*, *30*(8), 1429. https://doi.org/10.1029/2002GL016383

Zeng, Y. (2001). Viscoelastic stress-triggering of the 1999 Hector Mine earthquake by the 1992 Landers earthquake. *Geophysical Research Letters*, *28*(15), 3007–3010.